Applied Mathematical Modelling 39 (2015) 838–850

Contents lists available at ScienceDirect

Applied Mathematical Modelling

journal homepage: www.elsevier.com/locate/apm

Design trade-off study between efficiency and rotor forcing attenuation in a transonic turbine stage

Ricardo Puente [a,*], Guillermo Paniagua [b], Tom Verstraete [b]

[a] School of Aeronautics, Universidad Politecnica de Madrid, Madrid 28040, Spain
[b] Turbomachinery and Propulsion Department, von Karman Institute for Fluid Dynamics, Rhode-Saint-Genese B-1640, Belgium

ARTICLE INFO

Article history:
Received 20 September 2012
Received in revised form 9 December 2013
Accepted 8 July 2014
Available online 21 July 2014

Keywords:
Rotor–stator interactions
Shape optimisation
Transonic turbines
Turbine vanes
Unsteady aerodynamics

ABSTRACT

A multi-objective optimisation procedure was applied to the 3D design of a transonic turbine vane row, considering efficiency and stator outlet pressure distortion, which is directly related to the forcing induced in the rotor. The characteristic features that define different individuals along the Pareto Front were described, analysing the differences between high efficiency airfoils and low interaction. Pressure distortion was assessed by means of a model that requires only of the computation the steady flow field in the domain of the stator. The reduction of aerodynamic rotor forcing was validated via unsteady multistage aerodynamic computations carried out with NUMECA *FINE*^{TM}/*Turbo*. A well known loss prediction method was used to perform total loss decomposition to quantify the influence on efficiency of reducing rotor forcing. Results show that when striving for efficiency, the rotor was affected by few, but intense shocks. On the other hand, when the objective was the minimisation of distortion, multiple shocks appeared.

1. Introduction

The objective of the present paper was the design and physical description of a high pressure turbine (HPT) vane operating in the transonic regime, which was aimed at reducing the interaction between rotor and stator, while preserving high efficiency. The main agent of turbine row interaction is the shock system that develops at the trailing edge of an airfoil. In spite of the common belief that reducing shock intensity will mitigate both rotor forcing and losses, this paper illustrates the physics governing both contradictory effects.

The relevance of the study is based on the increasing importance of row interaction effects in aero-engine systems. Current design trends focus on weight and size reduction in order to improve the efficiency of the whole aircraft, which can lead to reduced distance between components and a higher loading per stage. This implies increased flow perturbation per row and less space for its damping, which according to Li and He [1,2] can lead to forcing increments of first order importance. In order to tackle this problem, the inherent unsteadiness of the flow field should be taken into consideration in every stage of the design process, as proposed by Hodson et al. [3].

Several sources of flow unsteadiness have been identified, with comprehensive accounts found in Paniagua [4] and Payne [5]. These can be classified as pressure waves propagation or *potential effects*, viscous effects where convection of low momentum flow causes local pressure distortions, and shock waves. Supersonic flow is characterised by the limited

* Corresponding author.
E-mail addresses: ricardo.puente@upm.es (R. Puente), gpaniagua@me.com (G. Paniagua), tom.verstraete@vki.ac.be (T. Verstraete).

http://dx.doi.org/10.1016/j.apm.2014.07.003
0307-904X/

Nomenclature

α	tangential flow angle
$\bar{u}$	velocity field
$\dot{m}$	mass flow
Ψ	spectral decomposition of ψ
ψ	forcing function according to the steady single row model
τ	stagnation pressure loss over inlet stagnation pressure
θ	angular coordinate for the pitch-wise direction of a turbine
a	sound speed
M_{is}	isentropic Mach number
p_0	stagnation pressure
p_s	static pressure
r	radial coordinate
r_{20}	radial coordinate at 20% span
r_{80}	radial coordinate at 80% span
S	shock function
T_0	stagnation temperature
w	coordinate of distance following the geometry of the leading edge of the rotor
Y	stagnation pressure loss over outlet dynamic head
EPR	events per revolution
HPT	high pressure turbine
LE	leading edge
LRS	left running shock
RRS	right running shock
Opt L	loss optimised geometry
Opt U	unsteadiness optimised geometry
PS	pressure side
SS	suction side
TE	trailing edge
U	resulting unsteadiness after integrating the forcing function over the risk region

attenuation of propagated perturbations. Therefore, the interaction between blade rows in transonic turbine stages will be of higher importance than in subsonic stages. Barter et al. [6] investigated numerically the propagation of shocks across a stage, both considering and neglecting wave reflections between rows. Results showed that the stator's trailing edge shocks, when reflected from the rotor, do have an important impact on the vane's loading, but successive reflections back to the rotor pose an influence of second order. Barter argued that only the unsteady frequency component corresponding to the first harmonic of the excitation is relevant. However, Kammerer and Abhari [7] demonstrated experimentally the importance of higher order harmonics.

Work on this topic has been carried out in the past at the von Karman Institute. Vascellari et al. [8] identified numerically the particularities of 2D profile velocity distributions that give rise to the trailing edge shock system. Joly et al. [9] set as objective the minimisation of vane outlet inhomogeneities using multi-objective optimisation techniques, revealing that efficiency and unsteady forcing are conflicting objectives. Multiple shock reflections may result in a reduced forcing at the expense of higher loss. Joly et al. described a geometry which achieves the same efficiency as a baseline one, while also minimising the outlet pressure distortion. The pressure side was heavily modified, generating a narrower channel with a divergent passage. The sonic line shifted upstream, resulting in a larger acceleration at the pressure side, coupled with a straight suction side rear part. This resulted in a reduction of the pressure difference at the trailing edge.

Previous research was focused in the study of 2D profiles, an approach that is not applicable to low aspect ratio turbomachinery flows, which are highly three-dimensional. Wang [10] concluded that the design of a 3D structure cannot be decoupled into 2D subproblems.

The novelty of the current research is the identification of various 3D flow field features present in an HPT vane that leads to low aerodynamic forcing in the downstream rotor, compared to a high efficiency one. The perspectives of improving both aspects are also explored.

2. Optimisation methodology

In order to reduce stator induced forcing in a turbine's rotor by a traditional design method, several trial and error iterations would be necessary. By designing a geometry using computational design and optimisation techniques, access is directly granted to a well performing geometry which can be investigated at length. Two objectives were set for the optimisation, efficiency and a measure of pressure distortion which will be described in detail in Section 4.1.

The optimisation problem can be mathematically formulated as the minimisation of some objective functions over a design space, while satisfying some constraint functions. The design space is the set of parameters that define the geometry of the turbine.

In the present multi-objective problem, both objectives conflicted with each other. In order to gain insight over their relationship, the concept of Pareto optimality was used. The Pareto Front is defined as the set of designs whose improvement with respect to one objective results in damage to the other one. By analysing designs far from each other in the Pareto Front, particular features of each solution can be described.

The optimisation code currently in use at the von Karman Institute is based on a Multi Objective Differential Evolutionary algorithm developed by Price and Storn [11]. Starting from an initial population, the performance of each individual is evaluated. Then, the whole population is sorted out by a ranking method, and a new population is proposed. The process is repeated for a specified number of *generations*.

3. Geometry and physics modelling

3.1. Airfoil parametric definition

The geometry generation strategy followed consists of parametrising blade to blade sections, and applying a stacking law to build the full 3D blade. Regarding endwall geometry, is was maintained constant and defined as axisymmetric in order to limit the scope of the study, as its contouring noticeably affects the pressure field [10].

Following the methodology proposed by Pierret [12], 2D sections are defined with a camber line, suction side (SS) and pressure side (PS) curves as depicted in Fig. 1a. The airfoil geometry is built using Bézier polynomials. Hence, the degrees of freedom are not actual points on a curve, but the vertexes of the so called control polygon. The advantage of using this approach is that Bézier curves ensure a high degree of differentiability, leading to a smooth aerodynamic response. In the case of the camber line, a base segment is defined using the axial chord and stagger angle. At the boundary points of these segments, the tangents coincide with the inlet and outlet metal angles. The camber line is then divided in pieces using a stretching law, which differs for constructing the SS and the PS curves. The normal distances d_1, d_2 and d_3 from the SS

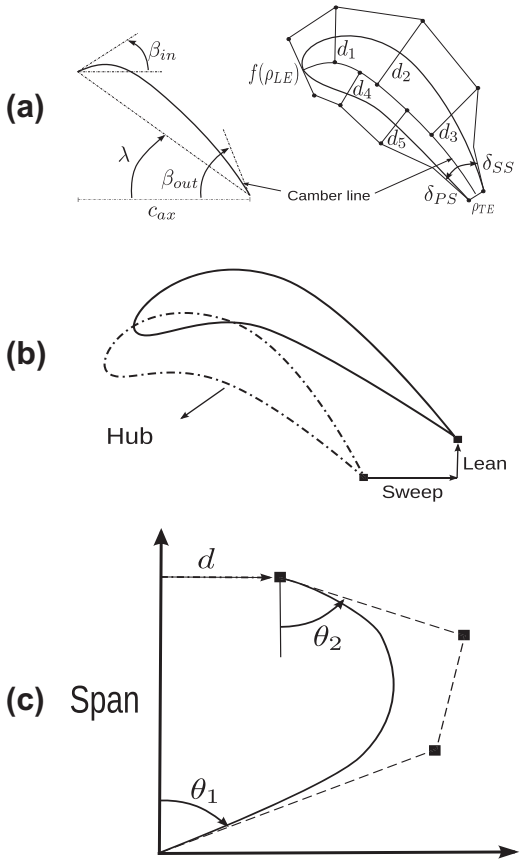

Fig. 1. Blade parametrisation.

stretched distribution determine the positions of the vertex of the control polygon that defines the SS curve. Likewise, the normal distances d_4 and d_5 define the PS curve. These curves are joined at the leading edge (LE) with second order continuity through placing the second control point of the SS and PS curves perpendicular to the camber line at the LE, guaranteeing the same LE curvature by constraining the relationship between these distances. This LE curvature radius is as well a design parameter. At the trailing edge (TE), the tangents on the SS and PS (δ_{SS} and δ_{PS}) are additional design parameters, which set the wedge angles to close the airfoil with a TE circumference, whose radius is imposed by manufacturing, structural, and thermal considerations.

In this work three profile sections were parametrised. In total, 10 parameters define a profile: 4 control points for the suction side, 3 for the pressure side, the leading edge radius, and the trailing edge's wedge angles. The inlet metal angle was imposed to be aligned with the inlet flow angle and the outlet metal angle was fixed at the desired outlet flow angle. Both axial chord and stagger angles were also fixed.

The stacking line was placed at the trailing edge in order to have higher control over the outlet flow topology. It was defined as the tangential (lean) displacement of the TE of each section with respect to the location of the TE of the hub profile (see Fig. 1b). To parametrise the lean, Bézier curves are again used. At four equidistant radial stations (hub, tip and two other radii in between), the positions of the Bézier control points were determined by the tip displacement, and the angles with the radial direction at hub and tip (see Fig. 1c). A fixed number of airfoils is considered, so that every geometry has the same pitch.

The three profiles and the stacking line add up to a total of 33 parameters to define a 3D airfoil.

3.2. Solver and mesh generation

Accurate CFD loss computation posed certain requirements, both in regards to mesh generation and flow modelling. Entropy generation mechanisms stem from viscous dissipation which require of a fine enough mesh in the wall region, and must not introduce unphysical privileged propagation directions. Meshes were generated through an automated structured grid generation routine.

The working hypothesis is that the pressure gradient acting on the rotor airfoils is dictated by the vane shocks, which in a first approximation can be considered stationary in the absolute frame of reference, and hence can be well predicted with steady state solvers. This point is further explained in Section 4.1. The Reynolds-Averaged Navier–Stokes code TRAF, developed by Arnone et al. [13], uses a Finite Volume spatial discretisation and a Runge–Kutta type time integration scheme to march in time towards a steady solution. Turbulence effects are accounted for with an algebraic Baldwin–Lomax model, considering the boundary layer as fully turbulent.

3.3. Boundary conditions and constraints

The boundary conditions of the vane are summarised in Table 1. Uniform flow was imposed at the inlet. At the outlet, an average static pressure was prescribed, determined by an objective value of isentropic Mach number.

The stator outlet plane was located where the following rotor's LE would be, namely, at $x/c_{ax,hub} = 0.4$ from the stator's TE. A restriction over the outlet angle was applied, formulated in Eq. (1). This equation represents a standard deviation between the actual outlet angle distribution and a prescribed one, limiting the constraint to the region not influenced by secondary flows, assuming that to be between the 20% and the 80% of the span. The average angle deviation is allowed to vary within a certain range. A perfect angle matching would result in a mass-flow of $\dot{m} = 8.91$ m/s.

$$\Delta\alpha = \sqrt{\frac{1}{r_{80} - r_{20}} \int_{r_{20}}^{r_{80}} \left[\alpha(r) - \alpha_{obj}(r)\right]^2 dr} < 1.5^\circ \tag{1}$$

4. Objectives definition

4.1. Pressure distortion model

The ultimate aim of reducing unsteadiness is to prevent harmful structural vibrations. The forced response of turbomachinery blades is usually computed using fluid–structure simulations, which can be either time resolved or linear harmonic decomposition methods, as used for example by Li and He [1] or by Escribano et al. [14] These calculations are very time consuming, thus infeasible to use in the context of a population based optimisation procedure. Assuming that the main

Table 1
Boundary conditions.

p_{01} (bar)	1.64
T_{01} (K)	440
$M_{is,2}$	1.25

component of rotor forcing is the non-uniformity of the pressure field induced by the stator, a model which uses only steady computations on a single row is hereby proposed.

The rotor airfoil traverses the non-homogeneous static pressure field dictated by the stator. In the rotor's reference frame, these inhomogeneities are felt like a time dependent inlet boundary condition, as depicted in Fig. 2, where with $\bar{w}$ denoting the direction of the rotor's leading edge.

The proposed pressure distortion model translates all the information of the steady static pressure field at the stator's outlet into a time dependent global forcing function on the rotor. Eq. (2) expresses the forcing function $\psi(\theta)$ as the average of the outlet pressure field in the direction of the rotor stacking, where w is the coordinate on a line parallel to the rotor's stacking line. Thus, $\psi(\theta)$ accounts for the total pressure forces felt by the rotor in terms of the pitch-wise coordinate θ. This function is non-dimensionalised by the inlet total pressure, and translated to the frequency domain as in Eq. (3).

The effect of the forcing function was assessed by checking against the rotor's Campbell diagram. In this diagram the structures' eigenfrequencies are plotted against engine revolutions. Lines representing a certain number of events per revolution (EPR) can be plotted as diagonal lines crossing the origin. Fig. 3 displays the corresponding Campbell diagram of the rotor airfoil. The aim is to minimise the amplitude of the forcing function in the risk region, defined by a lower (5400 RPM) and higher rotational speed (8000 RPM) that should allow a safe operation of the experimental turbine. The relevant frequencies are bounded to 9 kHz, higher order modes are neglected. As it can be seen in the figure, an excitation of the first bending mode occurring at approximately 6000 RPM cannot be avoided in the risk region.

The aerodynamic forcing was computed with a Nonlinear Harmonic Method implemented in the commercial solver NUMECA FINE/Turbo [15], by integration of unsteady pressure forces over the vane. This allows to validate the simplified pressure distortion model based only on a steady computation and assess if the rotor forcing is effectively reduced.

$$\psi(\theta) = \frac{1}{w_{tip} - w_{hub}} \int_{w_{hub}}^{w_{tip}} \frac{p_s(\theta, w)}{p_{01}} dw, \tag{2}$$

$$\Psi(EPR) = \int_{-\infty}^{\infty} [\psi(\theta) - \langle\psi(\theta)\rangle] e^{-ipEPR} d\theta, \tag{3}$$

$$U = \sum_{EPR_{max}}^{EPR_{min}} \Psi(EPR_i). \tag{4}$$

5. Results and discussion

The optimisation was set for a population of 40 individuals, the initial one being a random set. Fig. 4 shows the results. The two geometries at the extremes of the Pareto Front will be subject in what follows to detailed analysis, *Opt L* being the geometry with minimum losses, and *Opt U* the one which induces less unsteadiness in the rotor.

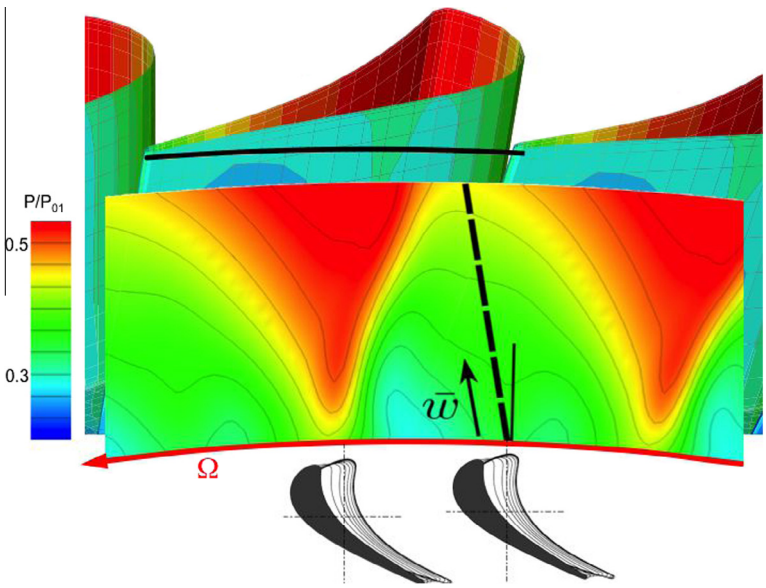

Fig. 2. Rotor crossing a non-homogeneous pressure field.

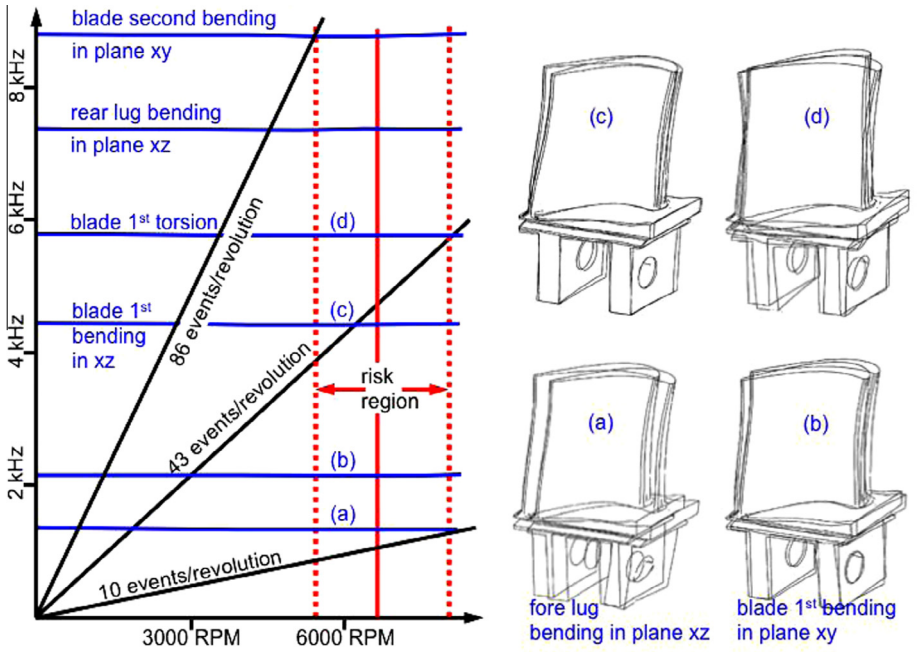

Fig. 3. Campbell diagram of the considered rotor. *X* is the radial direction, from hub to tip. *Y* is the tangential direction, in the rotor from PS to SS. *Z* is the rotating axis, from LE towards TE.

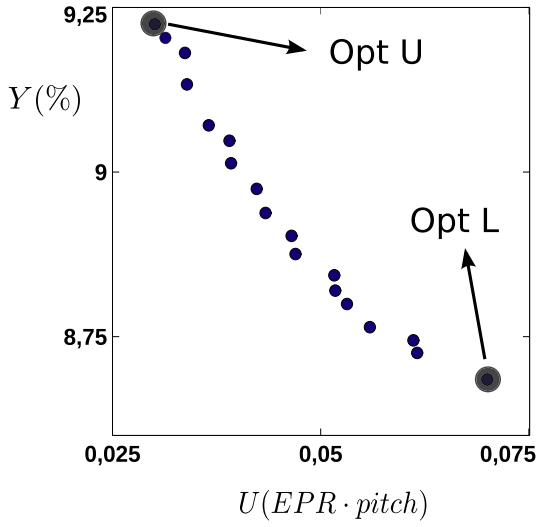

Fig. 4. Pareto Front.

Let us introduce two relevant variable fields, the Shock Function (see Eq. (5)) and the inlet based loss coefficient (see Eq. (6)). *S* is a scalar field which is positive in compression areas, above one in presence of shock waves, negative in expansion areas, and below one in expansion fans. Coefficient τ is appropriate for visualisation purposes, as the non-dimensionalising magnitude will be consistently the same for each analysed geometry. These variables allow the observed shock structures to be identified and characterised, linking them directly to loss generation mechanisms.

$$S(\bar{x}) = \frac{\bar{u}(\bar{x}) \cdot \nabla p(\bar{x})}{a(\bar{x})|\nabla p(\bar{x})|}, \tag{5}$$

$$\tau(\bar{x}) = \frac{p_{01} - p_0(\bar{x})}{p_{01}}. \tag{6}$$

5.1. Flow analysis at 10%, 50% and 90% span

In this section, an analysis of the flow field in three circumferential surfaces is carried out. Two near the endwalls, where secondary flows are of importance, and the mid-span section, where a quasi 2D behaviour is expected.

Shocks emerging from the SS are referred to as left running shocks (LRSs), from the PS as right running shocks (RRSs). RRSs will generally impinge on the SS of an adjacent blade and reflect towards the vane's outlet plane, marked by a vertical black line. Additional black lines in the throat area are $M_{is} = 1$ isolines, and denote the throat line and enclose supersonic flow pockets in otherwise subsonic flow regions. These features are named only in Fig. 5a and c, but they are sketched throughout.

Fig. 5 presents the pressure loss and shock function for the optimal turbine passage geometries at the hub. Regarding *Opt U*, the TE shocks (Fig. 5b) are strong enough to allow both the LRS and the reflection of the RRS to reach the rotor inlet plane, even though the reflected RRS is scattered by the wake. By contrast, for *Opt L* (Fig. 5), both the reflected RRS and LRS are damped by the wakes, and only one well defined shock wave arrives at the rotor inlet plane. The throat is shifted upstream for *Opt U* with respect to *Opt L*. Concerning the losses, when a shock impinges on a turbulent boundary layer, the sudden compression suffered by the low momentum fluid causes diffusion, and thus, a sudden growth of the boundary layer, which in turn causes compression waves. Therefore, this is a non-linear phenomenon, where the contribution to the result of each factor is difficult to anticipate. In this case, comparing plots Fig. 5a and c, it can be seen that after the impingement of the RRS, the boundary layer is thicker for *Opt U*. Nevertheless, no separation occurs for either airfoil.

Mid-span channel geometries are shown in Fig. 6, featuring an inflection point in the front part of the PS. Concerning *Opt L* (Fig. 6), successive reflections of the RRS on the SS and the wake heavily affect the development of the LRS. The outcome is finally two strong shocks reaching the rotor inlet. In *Opt U* (Fig. 6c), the situation is similar, but with less SS shock reflections, two weaker shocks reach the rotor inlet plane.

At the tip, shown in Fig. 7, the shock structures are simpler. The RRSs are particularly weak for *Opt L*, while for *Opt U* one notices a well defined and strong LRS and RRS. For the low forcing vane, the movement of the throat takes place only in the SS, being attached to the TE at the PS. Again, for the high efficiency vane, one strong shock reaches the rotor, whereas two weaker shocks do for the low forcing case.

Fig. 8 displays the isentropic Mach number distributions at 10%, 50% and 90% span. At the hub, the vanes are aft loaded, reducing the driving force of the secondary flows, exhibiting a strong acceleration in the rear portion of the vane passage. At mid-span and tip, in the efficient airfoils a strong acceleration occurs along the front part of the vane channel. Bearing in mind that the boundary layer grows with both free stream Mach number and flow acceleration [16], this implies an initially pronounced boundary layer growth. In turn, *Opt U* has a relatively constant flow acceleration, and the drop after the SS shock results in a lower velocity. Regarding the PSs, lower velocities are reached in *Opt L*, thus having a greater difference between SS and PS. At mid-span, the concavity of PS near the TE, reduces the acceleration, and the total effect is akin to that of a supersonic nozzle that tries to achieve uniform outlet conditions.

5.2. Outlet flow field and forcing analysis

Fig. 9a and b show each geometry and the outlet static pressure field non dimensionalised by the inlet total pressure. For *Opt L*, a single high pressure region is clear. Starting from the vertical dash-dotted line, following the direction of the rotor's sense of rotation, the pressure drops steadily until it rises suddenly. This is particularly apparent in Fig. 9c, where a shock

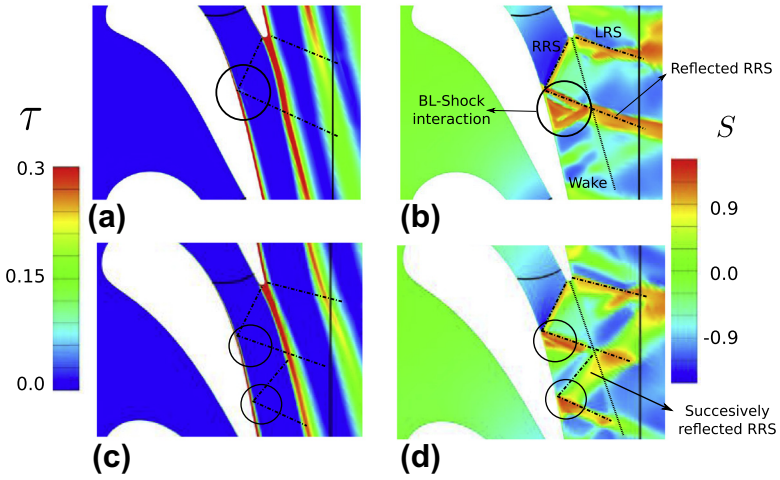

Fig. 5. τ and S fields at hub. Top, *Opt U*. Bottom, *Opt L*.

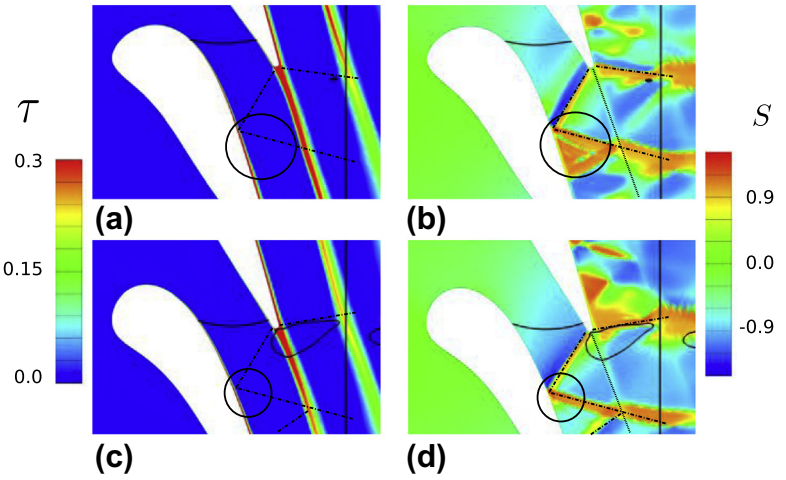

Fig. 6. τ and S fields at mid-span. Top, *Opt U*. Bottom, *Opt L*.

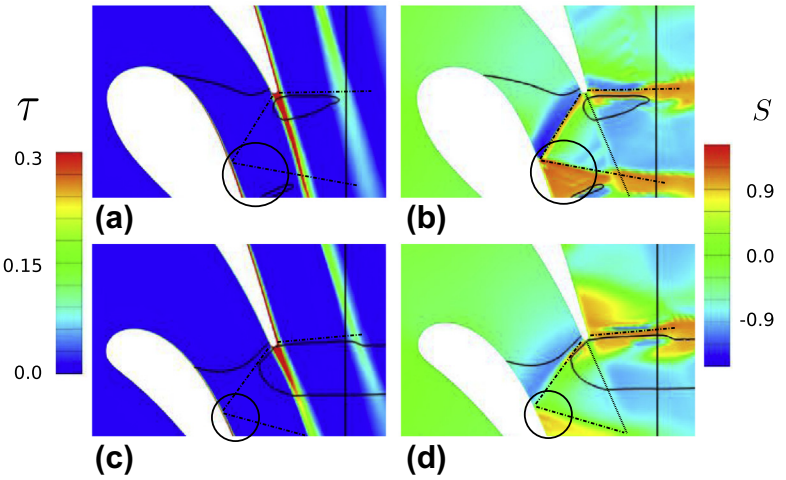

Fig. 7. τ and S fields at tip. Top, *Opt U*. Bottom, *Opt L*.

column signals the abrupt rise, with compression appendages penetrating into low pressure regions. In *Opt U*, two high pressure regions and their respective low pressure regions are present, limited by corresponding shock columns.

These pressure fields translate into the forcing function models and their spectral decomposition above in Fig. 10. *Opt L* shows decreasing spectral amplitudes. *Opt U* on the other hand presents a second harmonic which is stronger than the first. The same results are presented for the computed aerodynamic forcing below in the same figure. In order to present these data, the static pressure field over the rotor blades is extracted for 20 time steps per stator pitch from the unsteady multirow computations carried out with NUMECA *FINE*^{TM}*/Turbo*. The resultant of the force is computed, and non dimensionalised by the rotor's area multiplied by the total inlet pressure. The forcing function follows the trend of the computed aerodynamic forcing for both cases.

Making the analogy that the rotor is a moving object that encounters obstacles on its way, it is interesting to see what can be their size, number and how difficult they are to surpass. For that matter, Fig. 11 shows the isosurfaces of $M_{is} = 1$, which are relatively easy to overcome, and $M_{is} = 1.4$, more difficult. A translucent plane represents again the potential location of the rotor's LE. In *Opt L*, the higher speed flow regions are contained in pockets attached to the SSs behind the throat, and never threaten the rotor. However, supersonic flow is still contained within the large $M_{is} = 1$ structures, influencing the rotor along most of the span. In *Opt U*, the red surfaces are larger, but again, they do not pose a threat. Blue surfaces barely touch the postprocessing plane in this case.

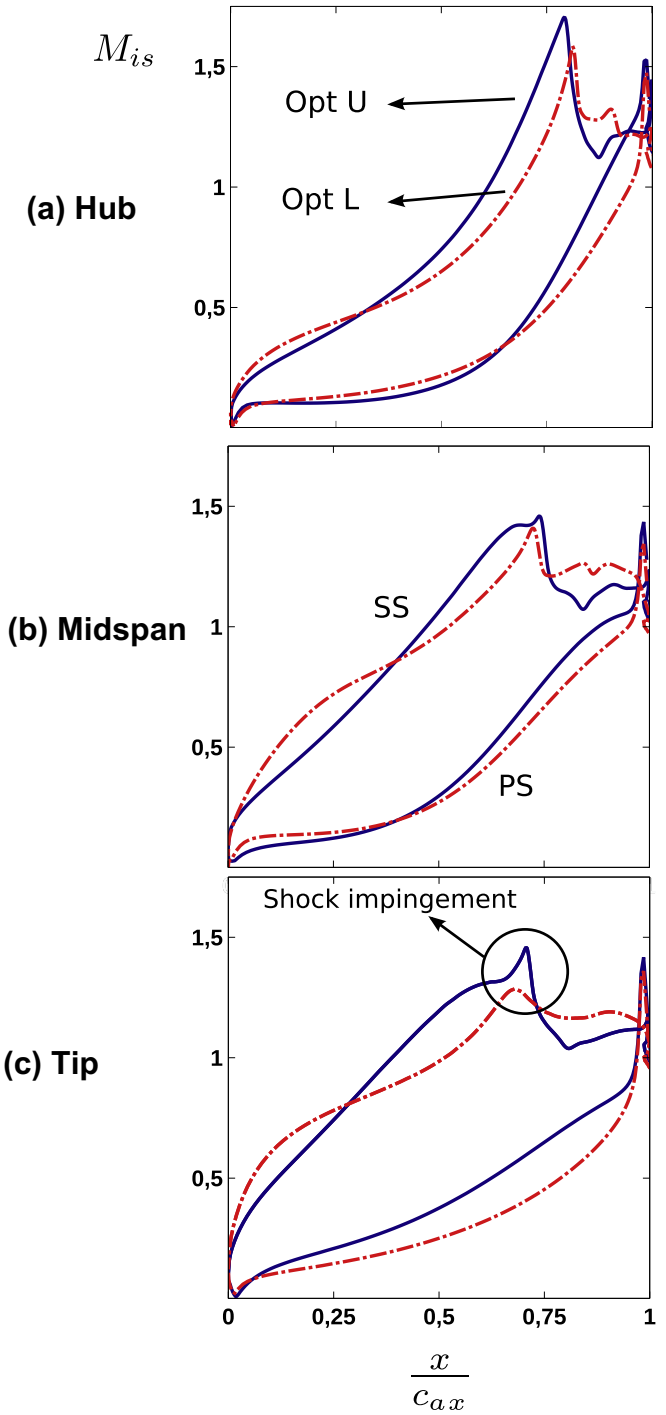

Fig. 8. M_{is} distributions.

5.3. Loss decomposition and circumferentially averaged analysis

This work will make use of a well known and widely used performance prediction method to assess loss levels, proposed by Kacker & Okapuu [17]. Loss is defined in terms of total pressure loss coefficient, as in Eq. (7). This system is a mean line performance prediction method, which means that it must be fed values at mid-span. The different mechanisms of loss generation are accounted for by adding up several loss components, as in Eq. (8):

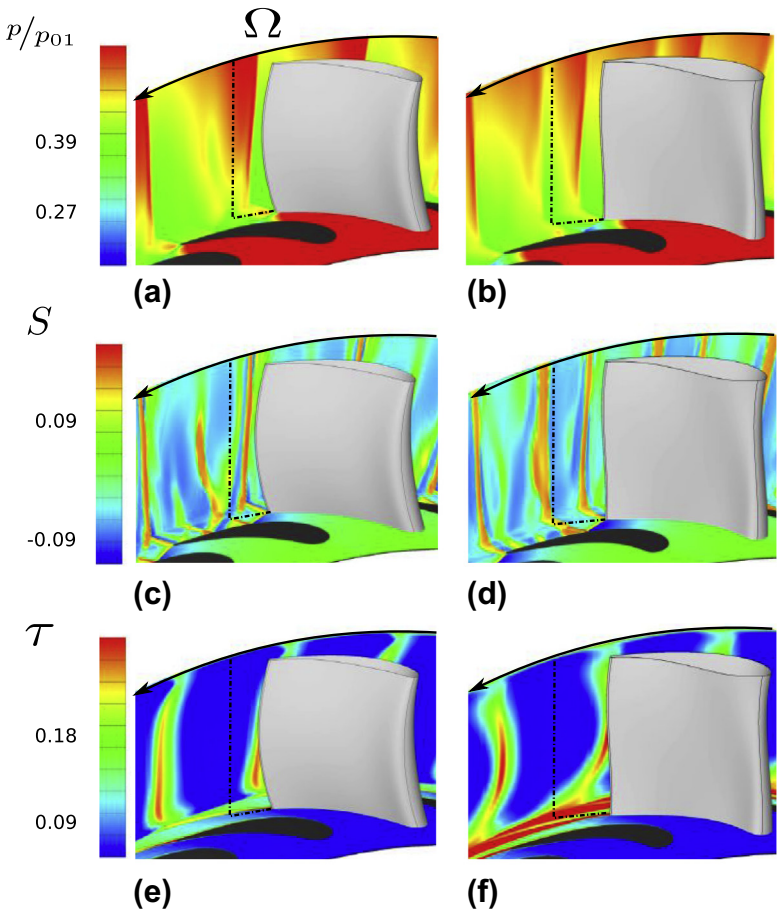

Fig. 9. Pressure, shock function, and loss coefficient fields at the outlet plane. Left, *Opt L* geometry. Right, *Opt U* geometry.

$$Y = \frac{p_{01} - p_{02}}{p_{02} - p_2} \tag{7}$$

$$Y_T = Y_p + Y_s + Y_{TET} + Y_{TC}. \tag{8}$$

Y_p gathers the influence of mid-span 2D geometry and flow field, Y_s accounts for the contribution of secondary flows, Y_{TET} provides with TE thickness (TET) blockage effects, and the term Y_{TC} means tip clearance losses. This last term will not be considered, as a vane does not have tip clearance.

In Table 2 a relation of each loss component is found for each geometry. The secondary loss components do not vary, which is confirmed by the CFD computed span-wise distributions in Fig. 12 right for *Opt L*, but not for *Opt U*. This geometry has heavy secondary losses at hub, which is not predicted by the correlations, due to an increased loading with respect to its efficient counterpart *Opt L*. The passage vortexes at hub and tip cause under-turning (see Fig. 12 left), and a local secondary loss decrease. The general tendency is a decrease of loss with going up along the span, which is consistent with both the outlet angle tendency. According to the correlations, the difference in efficiency is due to the influence of both profile losses and throat blockage, which is fully supported by CFD, as was seen during the previous analysis of airfoil 2D sections.

A summary of the CFD predicted performances are provided in Table 3. Note that the optimised configurations are able to ingest more mass-flow, demonstrating the potential of the design approach to reduce the shock unsteadiness onto the rotor, even being subject to higher demands.

5.4. Stacking line effect

Opt L exhibits a compound lean, being monotonously concave at the SS. This configuration decreases the pressure gradient between SS and PS at the endwalls, thus reducing the secondary losses. *Opt U*, on the other hand has a double compound lean with a convexity at hub that increases the pressure gradient, and explains the high secondary losses there. But this

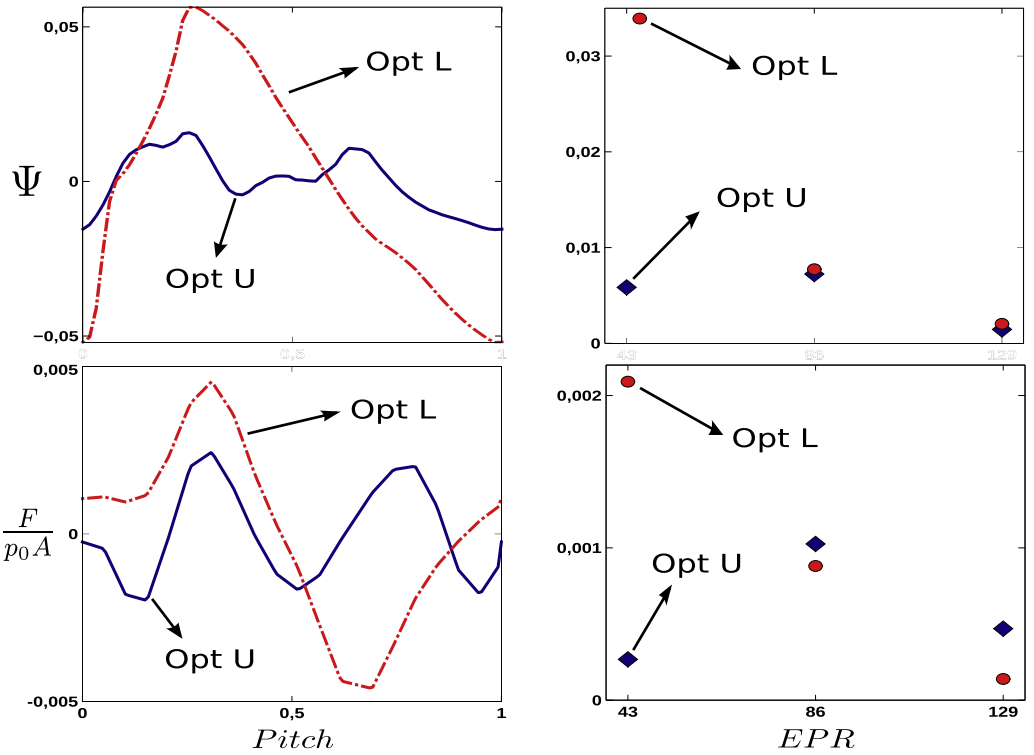

Fig. 10. Forcing functions. Above, model function. Below, computed unsteady forcing.

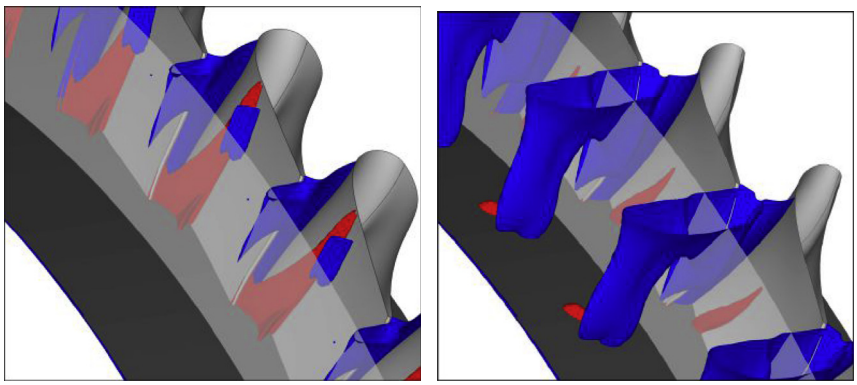

(a) Opt U geometry (b) Opt L geometry

Fig. 11. Isosurfaces of $M_{is} = 1$ (blue) and $M_{is} = 1.4$ (red). (For interpretation of the references to color in this figure legend, the reader is referred to the web version of this article.)

Table 2
Loss decomposition.

	Opt L	*Opt U*
Y_p (%)	2.88	2.89
Y_s (%)	5.39	5.39
Y_{TET} (%)	0.75	0.99
Y_T (%)	9.03	9.25

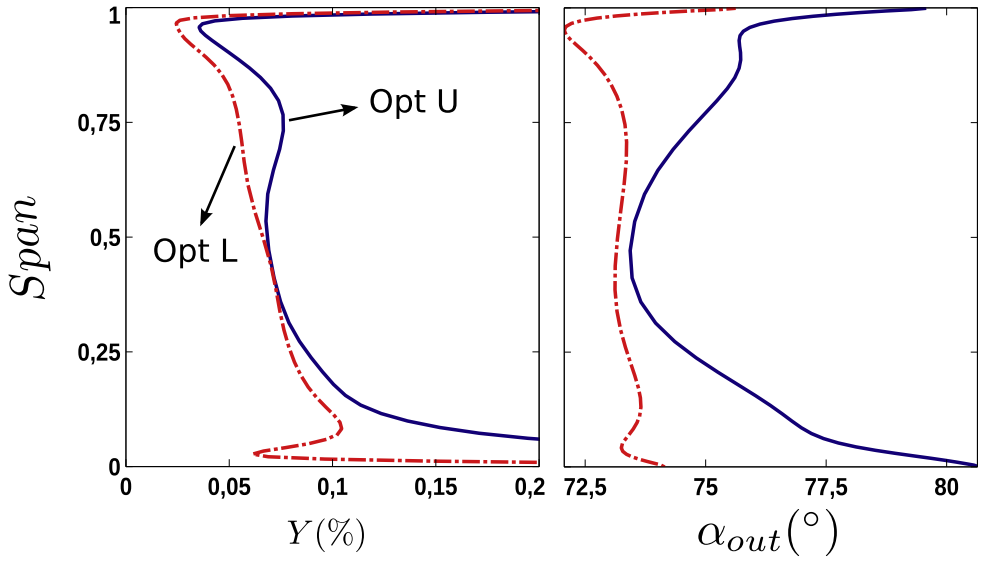

Fig. 12. Circumferentially averaged radial distributions.

Table 3
Computationally predicted performance.

	Opt L	*Opt U*
Y (%)	8.81	11.79
$\dot{m}$ (kg/s)	11.41	10.16
Objective mass flow deviation (%)	26.78	12.89

increased pressure gradient helps in the development of the strong shocks that characterise this geometry. In Fig. 9, in the lower row, it is seen that the loss field follows the lean.

6. Conclusions

A model of unsteady pressure excitations which requires only the steady computation of the upstream row is presented. This model is physically sound and has been validated against unsteady multirow computations, which are one order of magnitude higher in terms of computational expense. However, special care must be taken when defining the computational domain. The outlet plane should be identical to the postprocessing plane, located at the axial position of the leading edge of the downstream row.

These tools have been used to generate well performing turbine geometries in terms of induced rotor forcing and efficiency. Selected geometries from the extreme points of the Pareto Front of a multiobjective optimisation process show how efficiency is lost while reducing rotor forcing. These geometries are analysed and the relevant flow features, such as shock systems and interaction between shocks and viscous flow, are identified and described. Rotor forcing is reduced by smoothing the static pressure field by means of increasing the number and reducing the intensity of shocks.

The conclusion is that a great potential for rotor excitation reduction exists while still achieving high efficiency.

Acknowledgements

The authors would like to acknowledge the help provided by Z. Alsalihi and J. Prinsier by carrying out the unsteady multirow simulations and helping with the postprocessing. This work has also benefited greatly from the assistance of M. Joly through his know-how, and the insight gained during his previous work.

References

[1] H.D. Li, L. He, Blade aerodynamic damping variation with rotor–stator gap: a computational study using single-passage approach, J. Turbomach. 127 (2005) 573–579.
[2] H.D. Li, L. He, Towards intra-row gap optimization for one and a half stage transonic compressor, J. Turbomach. 127 (2005) 589–598.
[3] H.P. Hodson, T.P. Hynes, E.M. Greitzer, C.S. Tan, A physical interpretation of stagnation pressure and enthalpy changes in unsteady flow, in: Proceedings of the ASME TurboExpo.

[4] G. Paniagua, Investigation of the Steady and Unsteady Performance of a Transonic HP Turbine (Ph.D. thesis), Université Libre de Bruxelles, 2002.
[5] S.J. Payne, Unsteady Loss in a High Pressure Turbine Stage (Ph.D. thesis), University of Oxford, 2001.
[6] J.W. Barter, J.P. Chen, P.H. Vitt, Interaction effects in a transonic turbine stage, in: ASME, Proceedings of the ASME TurboExpo, vol. 2000-GT-0376.
[7] A. Kammerer, R.S. Abhari, Blade forcing function and aerodynamic work measurements in a high speed centrifugal compressor with inlet distortion, in: Proceedings of the ASME TurboExpo.
[8] M. Vascellari, R. Dénos, R.V. den Braembussche, Design of a transonic high-pressure turbine stage 2d section with reduced rotor/stator interaction, in: ASME, Proceedings of the ASME TurboExpo, vol. GT2004-53520.
[9] M. Joly, T. Verstraete, G. Paniagua, Attenuation of vane distortion in a transonic turbine using optimization strategies, in: ASME, Proceedings of the ASME TurboExpo, vol. GT2010-22370.
[10] Z. Wang, Three-Dimensional Theory and Design Method of Bowed-Twisted Blade and its Application to Turbomachines, Turbomachinery Blade Design Systems, VKI Lecture Series, 1999.
[11] K. Price, N. Storn, Differential Evolution – A Simple and Efficient Adaptive Scheme for Global Optimization Over Continuous Spaces, Technical Report TR-95-012, University of California, 1997.
[12] S. Pierret, Designing Turbomachinery Blades by Means of the Function Approximation Concept Based on Artificial Neural Network, Genetic Algorithm, and the Navier Stokes Equations (Ph.D. thesis), Faculté Polytechnique de Mons, 1999.
[13] A. Arnone, M.S. Liou, L.A. Povinelli, Integration of Navier–Stokes equations using dual time stepping and a multigrid method, AIAA 33 (1995) 985–990.
[14] A.G. Escribano, A. Serrano, C. Vasco, Cascade-gust interaction problem analysis based on linear cfd calculations, in: 4th CAA Workshop on Benchmark Problems.
[15] F. Wilquem, FINE Turbo v8 Manual: Unsteady Treatment, Non-Linear Harmonic Method, NUMECA International, 2008.
[16] D.L. Whitfield, Integral Solution of Compressible Turbulent Boundary Layers Using Improved Velocity Profiles, Technical Report AEDC-TR-78-42, Arnold Engineering Development Center, 1978.
[17] S.C. Kacker, U. Okapuu, A mean line prediction method for axial flow turbine efficiency, J. Eng. Power 104 (1982) 111–119.